Tectonophysics 865 (2023) 230042

Contents lists available at ScienceDirect

Tectonophysics

journal homepage: www.elsevier.com/locate/tecto

Coseismic slip and deformation mode of the 2022 *M*w 6.5 Luding earthquake determined by GPS observation

Hongbao Liang [a], Yanqiang Wu [a,*], Zhigang Shao [b], Jingwei Li [a,f], Yalun Li [c], Songquan Yi [c], Fan Yang [d], Wenquan Zhuang [d], Hua Wang [e], Wei Zhan [a], Changyun Chen [a]

[a] *The First Monitoring and Application Center, CEA, Tianjin, China*
[b] *Institute of Earthquake Forescating, CEA, Beijing, China*
[c] *Crustal Deformation Monitoring Center of Sichuan Earthquake Agency, Ya'an, China*
[d] *The Second Monitoring and Application Center, CEA, Xi'an, China*
[e] *Guangdong University of Technology, Guangzhou, China*
[f] *Innovation Academy for Precision Measurement Science and Technology, CAS, Wuhan, China*

A R T I C L E I N F O

Keywords:
Coseismic slip
Deformation mode
Rupture propagation
Seismic hazards
GPS

A B S T R A C T

The Luding *M*w 6.5 earthquake on September 5, 2022 occurred in the southeast section of the Xianshuihe Fault, filling a seismic gap previously identified by the earthquakes (M > 6.5) since 1700. The horizontal coseismic displacements are obtained using remeasurement data from global positioning system (GPS) campaign stations over a range of ~80 km from the epicenter. The overall pattern of displacements is consistent with left-lateral strike-slip. The largest displacement (~ 227 mm in the north-north-east direction) is observed at station ZD17, located ~10 km east of the epicenter. Coseismic slip distribution primarily propagates to the south-southeast of the epicenter, corresponding to the interseismic locking area. The lower stress accumulation of the north-northwest direction of the epicenter may arrest the rupture propagation. Slip located at shallower depths (1–3 km) is systematically smaller than that at deeper depths (4–8 km), suggesting a moderate shallow coseismic slip deficit. The distributed inelastic deformation caused by strong ground motion might be the main reason for the shallow slip deficit. The Daofu–Kangding section of the Xianshuihe and the Shimian–Mianning section of the Anninghe faults received a significant Coulomb stress increase caused by the Luding earthquake, and remained unbroken and hazardous.

1. Introduction

The Xianshuihe Fault was formed during the late period of the Songpan–Ganzi orogeny and is a part of the main structural belt in the Sichuan–Yunnan region on the southeastern margin of the Tibetan Plateau (Deng et al., 2003; Tapponnier et al., 2001). Together with the southern faults, which include the Anninghe-Zemuhe and Xiaojiang faults, it forms a large-scale left-lateral strike-slip fault system with a length exceeding 1000 km and plays an important role in the late Cenozoic crustal deformation of the eastern Tibetan Plateau (Wan et al., 2022; Wang et al., 2008). Since the Holocene, the Xianshuihe Fault zone has been characterized by strong left-lateral strike-slip movement. The long-term slip rates estimated from the interseismic velocity field measured by the global positioning system (GPS) correlate well with those estimated by tectonic geomorphology in the late Quaternary, which is approximately 6–12 mm/a (Allen et al., 1991; Bai et al., 2021; Li et al., 2022a; Qiao and Zhou, 2021; Shen et al., 2005). Owing to the strong tectonic movement, the Xianshuihe Fault zone is one of the most seismically active regions in western China. On September 5, 2022, the Luding earthquake occurred in the Kangding–Shimian segment (hereafter referred to as the Moxi Fault) of the Xianshuihe Fault (China Earthquake Networks Center CENC, 2022). Located at the confluence of the Xianshuihe–Anninghe–Longmenshan Fault basin, the active tectonics setting of the Luding earthquake is exceptionally complex, characterized by strong compressional left-lateral strike-slip movement (Jiang et al., 2015). Over the past 300 years, three strong earthquakes (M 7.0 in 1725, M 7.5 in 1955, and M 7.6 in 1786) occurred in the southern section of the Xianshuihe Fault from north to south (Wen et al., 2008). Luding earthquake occurred in the seismic gap of the southern extension of the fault. Therefore, investigating coseismic slip and

* Corresponding author.
E-mail address: chdqyw@126.com (Y. Wu).

https://doi.org/10.1016/j.tecto.2023.230042
Received 9 May 2023; Received in revised form 21 August 2023; Accepted 18 September 2023
Available online 21 September 2023

deformation mode is of great significance for understanding the seismogenic mechanism underlying the large strike-slip faults in the inner region of the plate and evaluating the seismic hazards of the surrounding major faults.

The near-field coseismic displacement captured by GPS and interferometric synthetic aperture radar (InSAR) can accurately describe the distribution of coseismic deformations and provide reliable constraints for the slip distribution; hence, near-field coseismic displacement observations are widely used to investigate source characteristics (Ding et al., 2018; Feng and Sigurjón, 2012; He et al., 2016; Jiang et al., 2014; Liu et al., 2022; Massonnet et al., 1993; Song et al., 2019; Zhang et al., 2023a; Zhao et al., 2018). The InSAR data are highly incoherent due to the significant relief and high vegetation coverage in the Luding area. In addition, the north–south strike of the Moxi Fault is approximately parallel to the satellite orbit; therefore, the coseismic displacements from Sentinel-1 ascending track could not be well obtained. To accurately determine the coseismic displacement distribution of the Luding earthquake, 18 campaign GPS stations with epicenteral distance of ~80 km were re-observed from September 6 to 19, 2022. The horizontal coseismic displacement field comprising 29 GPS stations was obtained using continuous GPS stations within ~200 km. We investigated the detailed rupture process of the 2022 Luding earthquake from the coseismic displacements. Based on the results of the three-dimensional (3D) deformation field and velocity profile during the interseismic period, we analyzed the seismogenic mechanism, and seismic hazards of the surrounding faults.

2. Coseismic displacements distribution

2.1. GPS observation

The Luding earthquake occurred at 04:52 (UTC) on September 5, 2022. We selected 11 continuous GPS stations with epicentral distances of ~200 km and 18 campaign stations with epicentral distances of ~100 km to derive the coseismic displacements. Usually, the coseismic displacement can be retrieved from the two successive days covering the occurrence of the earthquake. However, the reliability of coseismic displacement calculated from only two-day data may be low due to the noises and gross errors in the GPS coordinate time series. If the coordinates of a given day have significant gross errors, then it takes at least three-day data to determine reliable coordinates. In addition, the rapid afterslip may occur after the main shock. Therefore, the coseismic displacement was estimated six days before and three days after the earthquake. Finally, the continuous GPS data was selected from August 30 to September 7, 2022, and the initial 5 hours prior to the earthquake on September 5 was removed because the coordinate precision was lower than the coordinate precision calculated from 24 h observation data. The campaign stations were observed for at least three sessions (more than two sessions before the earthquake and one after the earthquake). The last period of data before the earthquake was observed within approximately four months (from May 1 to August 30), and most stations after the earthquake were observed within 14 days (from September 6 to September 19). Geodetic Trimble and TPS series instruments were used in campaign observation, and the time length exceeded 72 hours in each period.

The observation data of 29 GPS stations and approximately 157 International GNSS Service (IGS) stations were processed using the GAMIT/GLOBK software (version 10.70) (Herring et al., 2018a, 2018b), and the unified solution strategy and chosen models were adopted (Liang et al., 2022). The coordinate time series of 29 GPS stations were obtained to estimate coseismic displacements. The coseismic displacements of 29 GPS stations were estimated by fitting the multi-period coordinate series with a linear piecewise function model (Fig. 2 and Fig. 3), the model is as follows:

$$y^C(t_i) = c_1 + c_2 t_i + gH(t_i - T) \tag{1}$$

where $y^C(t_i)$ is the computed value of one of the coordinates (north, east), t_i is the i th epoch of the series, c_1 is the initial position, c_2 is the linear rate of motion, g is the coseismic displacement, T is the time of Luding earthquake, and H is the Heaviside function.

2.2. Coseismic displacement

The aperture of coseismic displacement was approximately 170 km in the quasi-north-south direction of the parallel fault zone, approximately 120 km in the quasi-east-west direction of the normal fault zone, and approximately 80 km in the direction of the parallel fault zone where the displacement exceeded 10 mm. A maximum displacement of ~227 mm toward the northeast was observed at the ZD17 station, ~10 km east of the epicenter. Along the strike of the seismogenic fault, the stations on both sides moved in opposite directions, indicating a type of left-lateral strike-slip. The displacements of the stations located in the northeast and southwest directions of the epicenter were larger than those located in the northwest and southeast directions of the epicenter, showing a small tensile component. For example, the displacement of the H073 station moving to the northeast was larger than that of the H074 station moving to the southeast, and the displacement of the CP10 station moving to the southwest was larger than that of the SCSM station moving to the northwest (Fig. 1a).

3. Coseismic slip inversion

As known, the vertical coseismic displacement can provide better constraints on fault dip and rake. Unfortunately, GPS vertical displacement was not used in the coseismic slip inversion of this work, mainly based on the following factors: The coseismic signals of GPS continuous stations far from the epicenter are tiny, and the coseismic displacements of campaign stations near the epicenter are less reliable because of the influence of the annual motion caused by environmental loads; The results of focal mechanisms (Table 1) show that the Luding earthquake is mainly strike-slip and the vertical displacement may not be obvious. So, under the constraint of only GPS horizontal displacements, a fault model for the 2022 Luding earthquake was constructed using the SDM software (Wang et al., 2013). The stress-drop smoothing constraint was applied to the slip of adjacent fault slices in the inversion. The vertical velocity structure of the crust has layered characteristics. In order to reduce the impact of inelastic deformation in the shallow crust on the inversion result, the top of the fault starts 1 km below the surface in the inversion using a purely elastic model. The displacements at station H363 were not used in the inversion owing to the large fitting residuals ($>$ 60 mm) in multiple trial inversion attempts. Field investigation found that the station is close to the seismogenic fault and located in a severe landslide area. In addition to the coseismic displacement, irregular deformation may also exist in station records. The displacements have also been shown in Fig. 3 for the convenience of future research.

According to various focal mechanisms (Table 1), tectonic setting (Deng et al., 2003), and the aftershocks distribution (Zhang et al., 2023b), the causative fault for the Luding earthquake was considered to be the Xianshuihe Fault with an NW-SE strike. The fault length was set to 50 km based on the distribution length of aftershocks in the NW–SE direction. The fault width was set to 20 km based on the focal depth range of various focal mechanisms ranging from 6 to 18.4 km. The strike and dip angle of the fault from the GCMT focal mechanism were used as the initial solution, and the rake angles were constrained by $-10°$–$10°$. The specific position and geometric features of the fault were retrieved via the grid search method. Finally, the positional coordinates of both ends of the fault were 29.751°N, 102.069°E and 29.318°N, 102.237°E, with strike and dip angles fixed at 161° and 86° (Fig. 4b and c). The smoothing factor was set as 0.08 from the trade-off curve (Fig. 4a). Fig. 4d shows the final slip distribution model, which was dominated by the left-lateral strike-slip, and the primary slip was located in the south-

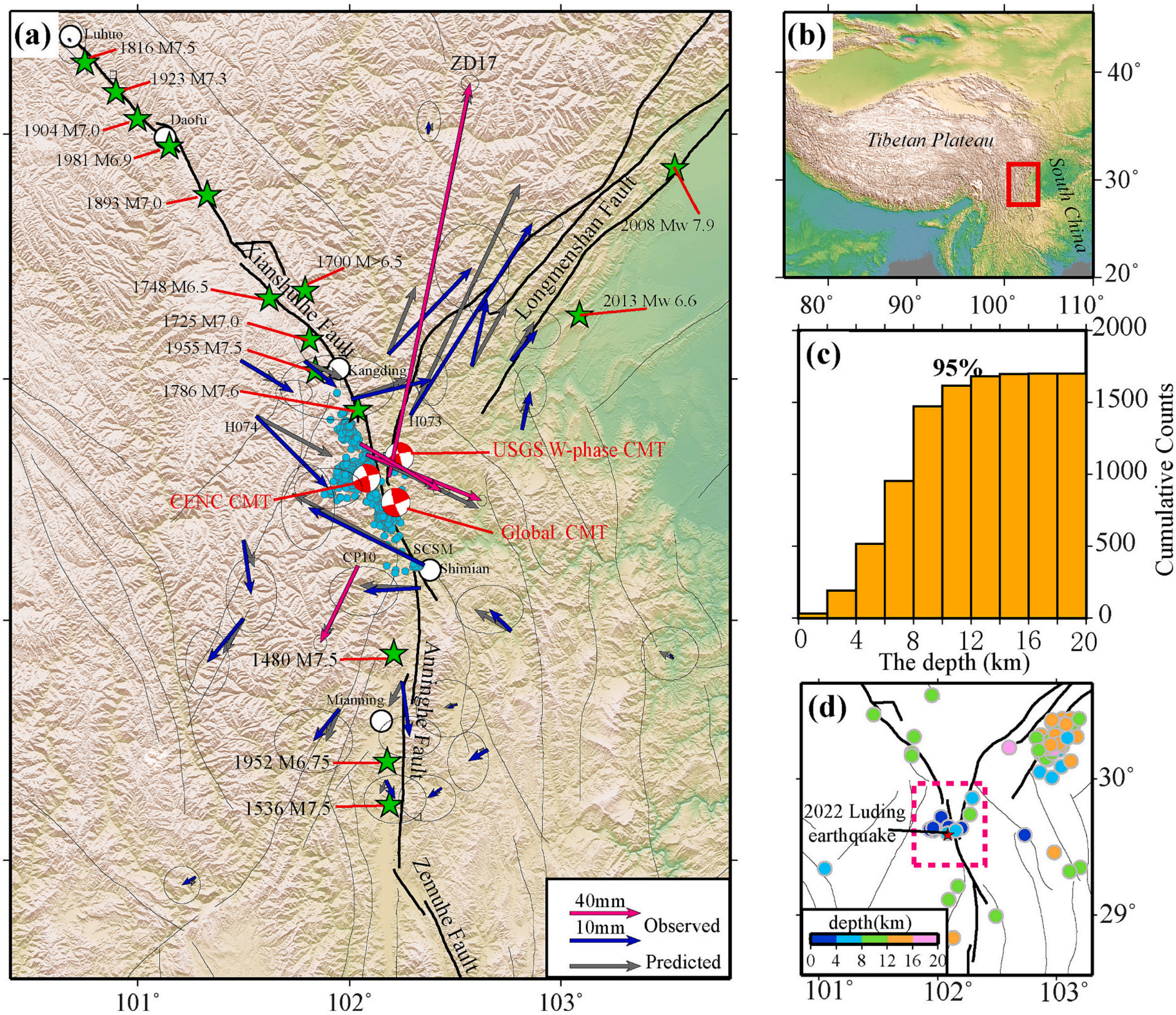

Fig. 1. Tectonic map of the southeastern Tibetan Plateau and coseismic displacements of the Luding earthquake. (a)The horizontal static GPS displacements. Error ellipses show 95% confidence levels. Bold black lines represent the Xianshuihe Fault (XSHF), Anninghe Fault (ANHF), and Longmenshan Fault (LMSF). Thin black lines indicate other active faults (Deng et al., 2003). The green stars represent the locations of the historical earthquakes (M > 6.5) since the year 1700 (Wen et al., 2008; Xu et al., 2019). The red beach ball represents the focal mechanism of the 2022 Luding earthquake (Table 1), and the cyan dots represent the aftershocks (Zhang et al., 2023b). The bold green line indicates the up-dip edge of the seismogenic fault of the Luding earthquake. The white dots indicate the location of the cities. (b)The area of Fig. 1a on the Tibetan Plateau. (c)The cumulative distribution of the depth of the main shock and 1700 aftershocks from September 5 to September 9, 2022 (Zhang et al., 2023b). (d)The $M \geq 2.5$ earthquakes that occurred between 2010 and 2020 (She et al., 2022). (For interpretation of the references to colour in this figure legend, the reader is referred to the web version of this article.)

southeast of the epicenter with the maximum slip of 1.65 m at a depth of ~6 km. The rupture area with slip >0.5 m was approximately 288 km^2 (24 × 12 km). The seismic moment was 7.2×10^{18} N·m, equivalent to a *M*w 6.5 earthquake. The data fitting was good (Fig. 1a). The correlation between GPS observations and model values was 99.64%. The root mean squares of residuals in the east–west, and south–north components were 2.3 mm and 2.4 mm, respectively.

To verify the reliability of the coseismic slip model, we performed a checkerboard test to check the resolution of GPS observations. The geometric parameters and the subfault size of the constructed fault planar were the same as those of the previous model inversion test. Since most of the slip of the model obtained from inversion was concentrated in a large slip patch (Fig. 4d), one slip patch was set in the checkerboard test. We assumed a slip patch ruptured on the fault with 9 × 6 subfaults and specified this with a 1 m purely left-lateral strike-slip (Fig. 4e). Simulated GPS horizontal displacements were calculated and then used to invert coseismic slip distribution with the same inversion method and smoothing factor as the real data inversion. The model-based slip distribution was well recovered (Fig. 4f), showing that the slip patch within the depth of ~12 km can be identified. The 3D elastic block model revealed a locking zone with an interseismic coupling coefficient (ISC) exceeding 0.6, extending from 0 to 12 km in depth (Li et al., 2021). In addition, the main shock and the 95% of aftershock depths were <12 km (Fig. 1c). The features could infer that the depth of the slip distribution was relatively shallow. Overall, these indicated that the GPS data used in this work was strong enough to reveal the shallow slip distribution on the fixed fault plane.

4. Discussions and conclusions

4.1. Comparison of coseismic slip models

We compare the coseismic slip model of the 2022 Luding earthquake with three representative models (Guo et al., 2023; Li et al., 2022c; Zhang et al., 2023b) in terms of data selection, fault geometry, and slip distribution. For data selection, Li et al. (2022c) constrains the coseismic slip by far-field GPS, strong-motion, and InSAR; Zhang et al. (2023b) adopt teleseismic P-wave and near-field strong-motion data; Guo et al.

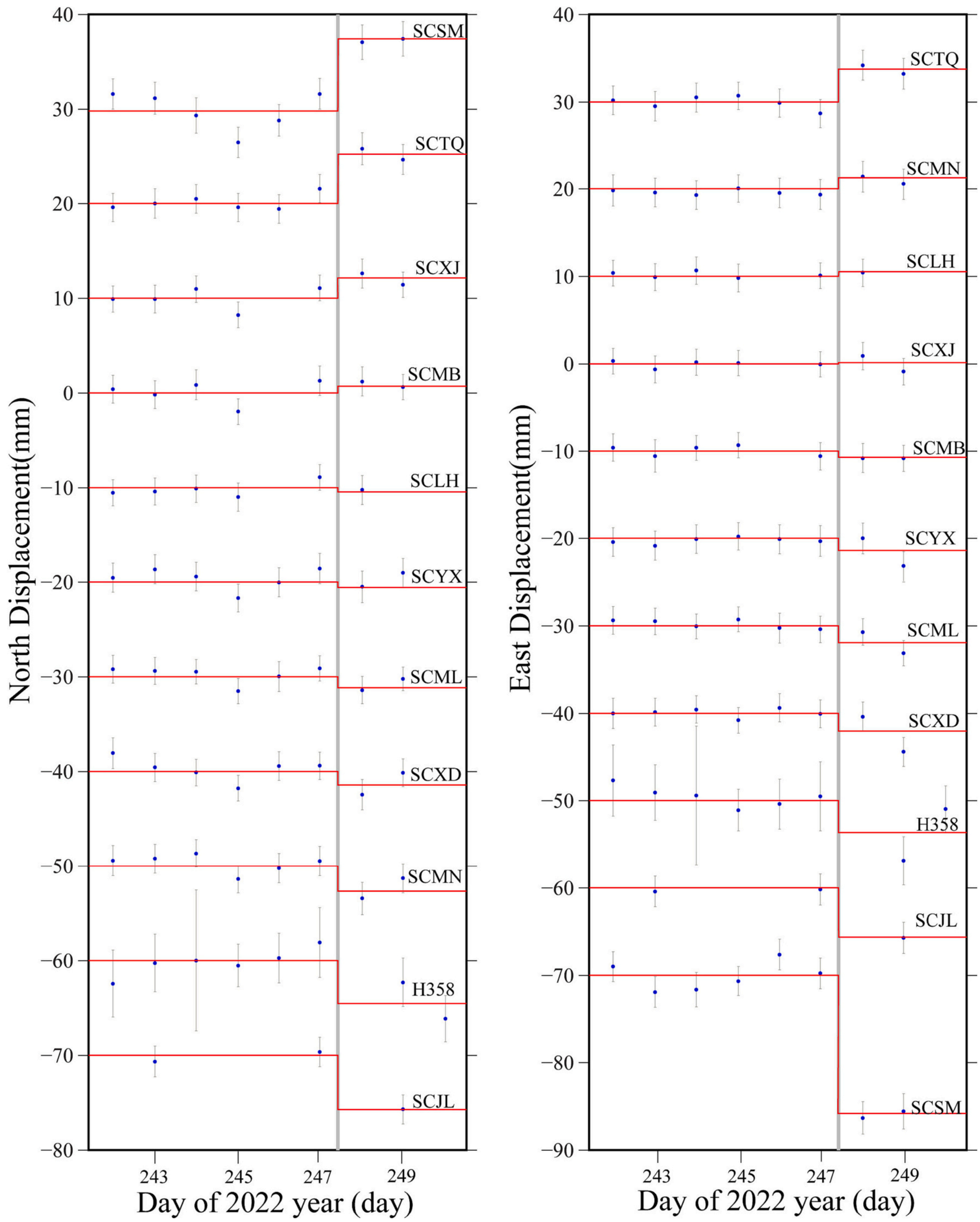

Fig. 2. The horizontal displacement time-series of GPS continuous stations.

(2023) utilizes almost all available data, such as teleseismic P and SH waves, local strong-motion waveform, far-field GPS, and InSAR; although only GPS data were used in our study, the most stations are <100 km away from the epicenter and 3 GPS stations distributed on both sides of the seismogenic fault are located within 10 km of the epicenter. For the fault geometry, Guo et al. (2023), Zhang et al. (2023b), and our results constructed a similar single-line fault model with a constant dip optimized by different data (Table 1) , while Li et al. (2022c) added a branch fault on the basis of the main fault, considering that the aftershocks to the northwest of the mainshock are clustered.

Though different in the constraint data, three published studies and our results show agreement in the dominant south-southeast rupture propagation and peak slip of 1.5–1.8 m at a depth of 6–8.6 km. However, differences exist in the details of slip distribution. The result of Li et al. (2022c) contain two major slip patch that is consistent with the result of Zhang et al. (2023b), but with a smaller shallow patch on the southern end of major rupture. Guo et al. (2023) inferred only one large slip patch that merges two separated subevents, which is consistent with our results. These comparisons are understandable and acceptable, because many factors can influence the inversion results, such as fault geometry, discretization of modeled fault, data type and its coverage, smoothing factor, crustal medium(e.g., layered and homogeneous), and dislocation theory (e.g., half space and earth spherical models). However, these comparisons can also be useful in assessing the contribution of slip

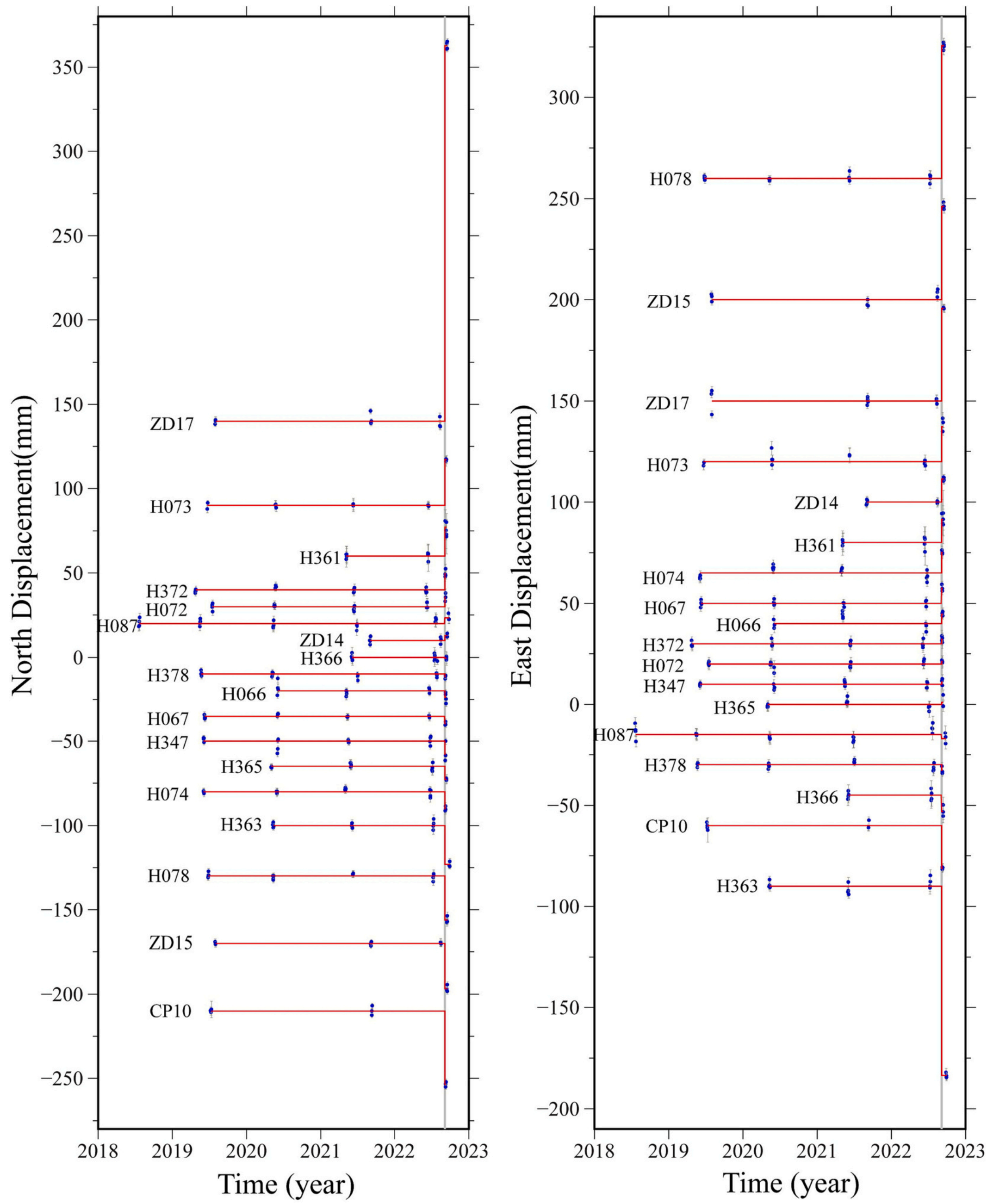

Fig. 3. The horizontal displacement changes of GPS campaign stations.

modeling to understanding the static rupture process. Overall, our results could capture the major kinematic feature of the 2022 Luding earthquake shown in the previous studies.

4.2. Depth distribution of coseismic slip

Significant differences were shown in the reported focal depths for the 2022 Luding earthquake, ranging from ~6–18.4 km, among research institutions and individuals (Table 1). This can be primarily attributed to the use of different observation data, crustal structures, and inversion methods. When near-station observation data (epicenter distance >10 km) do not exist, the depth error of traditional travel time positioning can exceed approximately 3 km (Fang et al., 2015; Gomberg et al., 1990). For the Luding earthquake, the focal depth inversion based on far-field waveform data was relatively deep, located between ~15–18.4 km (Table 1); however, the depth of the highly accurate relocation using >30 seismic stations within 50 km of the near-field was 9.3 km (Zhang et al., 2023b), which is close to the maximum slip depth obtained in this work.

The energy released by an earthquake is from the strain accumulation during the interseismic period, and the two correspond regionally (Avouac et al., 2015; Zhao et al., 2020). Based on the GPS observations of the Crustal Movement Observation Network in China (Wang and Shen, 2020), the precise deformation characteristics of the Moxi Fault were obtained using dense GPS stations observed between 2018 and 2022. The results show that the locking depth obtained from the velocity profile along the parallel direction of the fault was 5.36 ± 2.34 km (Fig. 5b), which is consistent with the depth (< 8 km) of seismicity around the ruptured area (Fig. 1d) and the maximum slip depth of ~6 km obtained in this work. Therefore, the depth of coseismic slip distribution obtained in this work is reasonable.

Previous studies have determined that the coseismic slip at shallower

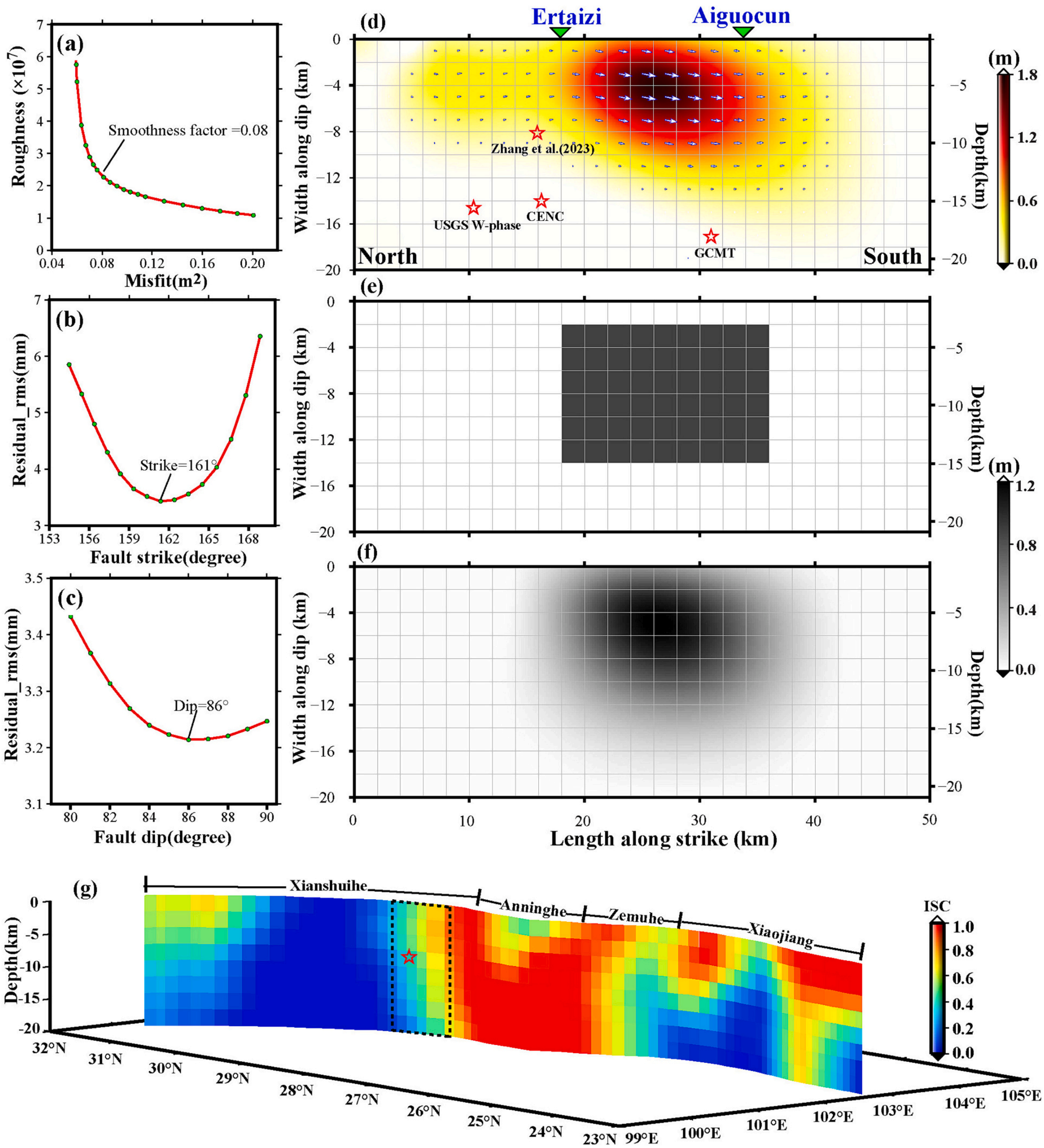

Fig. 4. Fault parameter tests, final slip model, checkerboard test and interseismic coupling. (a) The trade-off curve of relative fitting residual and roughness. The relationship between fault strike (b), dip (c), and fitting residuals. (d) Coseismic slip distribution of the 2022 Luding earthquake. (e) The input model with a slip patch, the slip magnitude with 9 × 6 subfaults was assigned as 1 m. (f) The model recovered by the GPS observations. (g) Interseismic coupling along the Xianshuihe-Anninghe-Zemuhe-Xiaojiang faults from Li et al. (2021). The rectangle with black dotted line in Fig. 4g represents the range of Fig. 4c.

depths (0–3 km) is systematically smaller than that at deeper depths (4–8 km), and this phenomenon is called the shallow slip deficit (SSD, Fialko et al., 2005). The SSD also occurred in the coseismic slip of the Luding earthquake (Fig. 4d). The maximum slip at shallow depth (1–3 km) was reduced by about 56% compared with that at deep depth (~6 km), which is similar to the typical strike-slip earthquakes, such as 1992 M 7.3 Landers, 2016 *Mw* 7.8 Kaikoura, and 2021 M 7.4 Maduo earthquakes (Fialko et al., 2005; Xu et al., 2018; Jin and Fialko, 2021). Various mechanisms have been proposed to explain the SSD. Xu et al. (2016) indicated that a lack of data constraints near the seismogenic fault would cause the shallow slip to be underestimated. The checkerboard test shows the resolution of the slip patch without SSD owing to the enhanced constraints of near-field GPS stations (Fig. 1a) in the reversion. The distributed inelastic deformation caused by strong ground motion also contributes to SSD (Kaneko and Fialko, 2011; Xu et al., 2018). The Luding earthquake triggered strong ground vibrations and the maximum of peak ground accelerations is 1368.53 cm/s^2 in the north, 873.92 cm/s^2 in the east, and 852.80 cm/s^2 vertical, respectively (Jiang et al., 2023), resulting a wide range of influence (~195 × 112 km) with the highest seismic intensity of IX (https://www.mem.gov.cn/xw/yjglbgzdt/202209/t20220911_422190.shtml). Surface rupture occurred in the Ertaizi-Aiguocun section of the Moxi Fault (Fig. 4d, Li

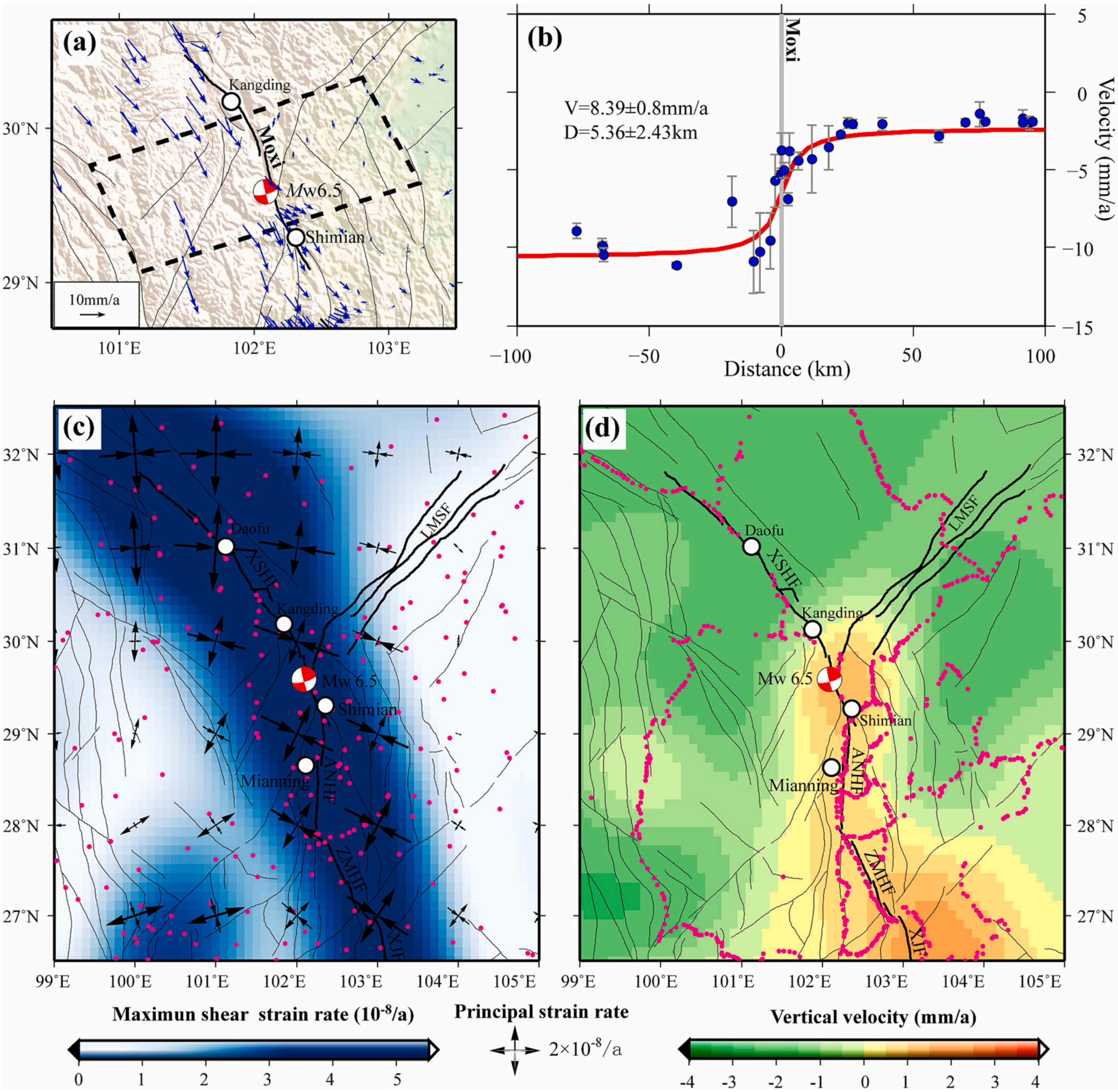

Fig. 5. Three-dimensional deformation during the interseismic period. (a) Dense GPS velocities with respect to the South China Block. Error ellipses show 68% confidence levels. (b)The GPS velocities in parallel directions of the Moxi Fault, with their locations shown in black rectangles in Fig. 5a. Red solid line represents the best-fitting curve using 2-D elastic dislocation model (e.g., Savage and Burford, 1973). (c) Horizontal principal and maximum shear strain rate fields based on GPS velocity field (Wang and Shen, 2020) were determined using the least squares collocation method (Wu et al., 2011). (d) Vertical velocity field observed jointly by Leveling and GPS data (Wu et al., 2022). The deep pink dots in Figure5c and 5d indicate the location of GPS/Leveling stations. (For interpretation of the references to colour in this figure legend, the reader is referred to the web version of this article.)

et al., 2022b), and a landslide with a total area of 17.36 km^2 occurred nearby (Huang et al., 2022). These results indicate that the shallow distributed inelastic deformation might be responsible for the SSD of the Luding event. Regarding the velocity-strengthening behavior in the shallow crust, the coseismic slip at the surface is expected to be suppressed compared to the slip at a deeper depth. The velocity-strengthening layer is, therefore, most directly manifested in a shallow interseismic creep and/or postseismic afterslip (Kaneko et al., 2013; LaBonte et al., 2009; Wei et al., 2015). Guo et al. (2023) believed that the interseismic shallow creeping is too tiny ($\sim$ 0.9 mm/a) to make up for the SSD. In addition, we cannot exclude whether the SSD was related to the postseismic afterslip due to lack of GPS observation.

4.3. Deformation mode during the interseismic period

In the epicenter of the 2022 Luding earthquake and its surrounding areas, the structure was relatively complex, and strong earthquakes were active. Understanding the role of these earthquakes in the process of interseismic stress accumulation and particularly determining whether these two recent strong earthquakes (2008 *Mw* 7.9 Wenchuan and 2013 *Mw* 6.6 Lushan earthquake) triggered the Luding earthquake is important. This information will help to explain the dynamic process from genesis to occurrence. Previous studies have demonstrated that the 2008 *Mw* 7.9 Wenchuan and 2013 *Mw* 6.6 Lushan earthquakes had a significant Coulomb stress loading effect on the Daofu-Kangding section of the Xianshuihe Fault, but had little effect on the Moxi Fault (Shan et al., 2013; Shao et al., 2010). In addition, GPS observations also verified that there was almost no strain rate change before and after the Wenchuan and Lushan earthquakes (Li et al., 2022a). Xu et al. (2019) analyzed the influence of historically strong earthquakes and tectonic movements on the Coulomb stress of the Moxi Fault. Although the 1786 M 7.6 earthquake produced a significant Coulomb stress unloading effect (> 1 MPa) on the Moxi Fault, the Coulomb stress changes associated with all three effects (coseismic, postseismic, and interseismic) have

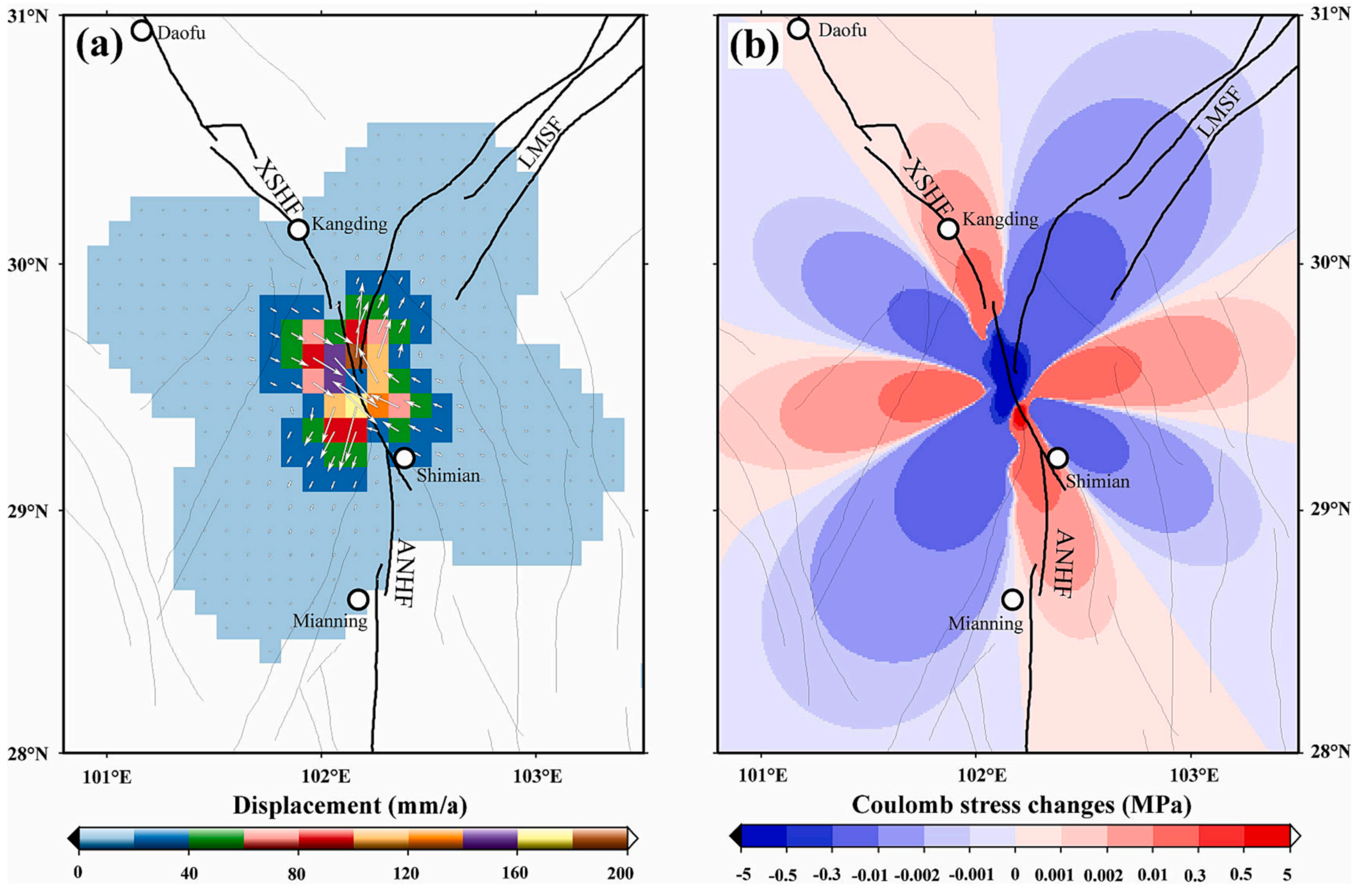

Fig. 6. Simulated coseismic displacement (a) and coseismic Coulomb stress change at a depth of 5 km (b) derived from coseismic slip model for the 2022 Luding earthquake obtained by this work.

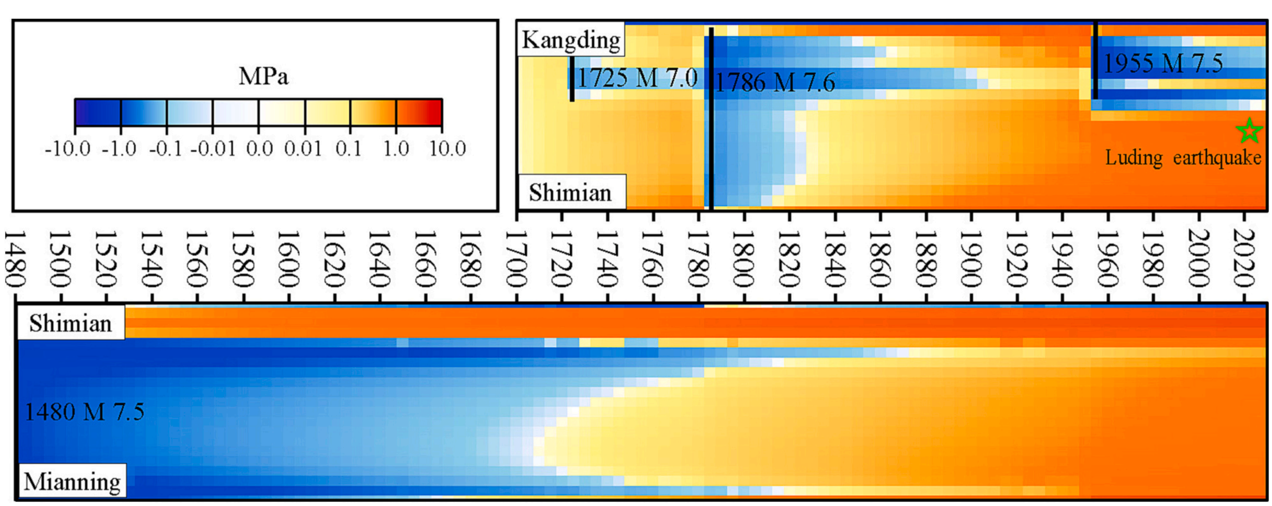

Fig. 7. Evolution of Coulomb stress changes associated with all three effects (coseismic, postseismic, and interseismic) along the strike direction of the Kangding–Shimian section of the Xianshuihe and the Shimian–Mianning section of the Anninghe faults (Xu et al., 2019). The vertical axis is the length of the fault from north to south, whereas the horizontal axis represents the evolution time. The thick black lines indicate where the strong earthquake occurred. The green star represents the location of the Luding earthquake. (For interpretation of the references to colour in this figure legend, the reader is referred to the web version of this article.)

exceeded 1 MPa (Fig. 7). Therefore, the stress accumulation released by the 2022 Luding earthquake was predominantly derived from regional tectonic movements.

The GPS interseismic movement can be interpreted as the tectonic movement. The horizontal velocities of GPS stations demonstrate a clockwise rotation with a large difference of ~10 mm/a between the two sides of the Xianshuihe–Anninghe–Zemuhe Fault (Wang and Shen, 2020); both the principal strain rate and the maximum shear strain rate along the fault zone were high. Statistical results indicate that 76.9% of earthquakes (M > 6.5) occurred in the region with a high strain rate of

Table 1
Focal parameters for Luding earthquake from different research institutions and individuals.

Auther	Data type	Epicenter			Focal mechanism			Moment magnitude (*Mw*)
		Longitude (degree)	Latitude (degree)	Depth (km)	Strike (degree)	Dip (degree)	Rake (degree)	
U. S. Geological Survey USGS (2022)	Global seismic wave	102.236	29.679	15.5	345	88	17	6.6
Global CMT Catalog Search GCMT, 2022	Global seismic wave	102.220	29.490	18.4	163	80	8	6.7
China Earthquake Networks Center CENC, 2022	Global and regional seismic wave	102.080	29.590	15.0	343	79	9	6.6
Zhang et al. (2023b)	Teleseismic P-wave data and near-field strong-motion	102.086	29.589	6.5	166	86	17	6.6
Li et al. (2022c)	Far-field GPS + InSAR + strong motion displacements	–	–	7.0	162 252	80 79	—— ——	6.7
Guo et al. (2023)	Teleseismic P and SH waves + strong motion waves + far-field GPS + InSAR	–	–	8.6	163	80	-4	6.6
This study	Near-field GPS	–	–	6.0	161	86	–	6.5

$>4 \times 10^{-8}$/a (Wu et al., 2021). The Luding earthquake occurred in an area with a high principal strain rate exhibiting a compression of $\sim 4 \times 10^{-8}$/a in the SE–NW direction, the tension of $\sim 2 \times 10^{-8}$/a in the NE–SW direction, and a high maximum shear strain rate of $\sim 5 \times 10^{-8}$/a (Fig. 5c), indicating that the strain energy of the seismogenic fault accumulated faster during the interseismic period. Meanwhile, the eastward movement of the materials in the Tibetan Plateau was blocked by the South China block, and the surface uplift of some areas along the fault may be attributed to the horizontal crustal shortening in its interior. The Luding earthquake occurred at the uplift area with a rate of ~1.5 mm/a (Fig. 5d), corresponding to the horizontal deformation feature of significant compression.

The coseismic rupture typically propagates to areas with high interseismic stress accumulation. The strong locking zones with an ISC of >0.4 have higher stress accumulation. Similarly, the weakly locking zones potentially inhibit the seismic rupture propagation (Kaneko et al., 2010; Vaca et al., 2018). The coseismic rupture of the 2022 Luding earthquake primarily propagated to the south-southeast of the epicenter (Fig. 4d), corresponding to the interseismic locking zones with an ISC of 0.4–0.8 (Fig. 4g). The weak locking zones (ISC < 0.4) located in the northwest of the epicenter (Fig. 4g) had low stress accumulation, likely related to the sustained stress unloading of the recent event (1955 M 7.5 earthquake) (Fig. 7), which potentially inhibited the seismic rupture propagation. Therefore, we can conclude that the coseismic slip mode for the Luding earthquake was largely related to the interseismic stress accumulation. The dislocation amount of seismogenic fault can be expressed as the product of the earthquake recurrence period and far-field loading rate (Schwartz and Coppersmith, 1984; Shimazaki and Nakata, 1980). This study reveals that the recurrence period of strong earthquakes in the Moxi Fault is approximately 200 years (Kato et al., 2007). The estimated maximum coseismic dislocation is approximately 1.68 m according to a slip rate of 8.39 mm/a measured by interseismic dense GPS stations (Fig. 5b). This value is close to the maximum coseismic dislocation of 1.65 m obtained by inversion in this work (Fig. 4d). Thus, it can be concluded that the interseismic and coseismic deformation are complementary.

4.4. Seismic hazards on surrounding faults

The loading effect of Coulomb stress caused by a large earthquake may trigger the occurrence of future earthquakes on the surrounding faults (Toda and Stein, 2020), such as the M 7.1 Luanxian earthquake 15 h later triggered by the 1976 M 7.8 Tangshan earthquake (Robinson and Zhou, 2005), and the 1999 *Mw* 7.1 Hector Mine earthquake triggered by the 1992 *Mw* 7.3 Landers earthquake (Freed and Lin, 2001). Based on the coseismic slip model of the 2022 Luding earthquake inverted in this work, the simulated coseismic displacements (Fig. 6a) and Coulomb stress changes (Fig. 6b) were calculated using PSGRN/PSCMP software (Wang et al., 2006). Coseismic displacements showed (Fig. 6a) that the rupture and unlocking of the Moxi Fault may accelerate the south-southeast movement of the Sichuan–Yunnan block, which may promote the strike-slip movement of the Kangding-Shimian section of the Xianshuihe Fault and the Shimian-Mianning section of the Anninghe Fault. Significant Coulomb stress loading occurred in the unruptured areas in the fault direction (Fig. 6b), with a maximum stress of >0.01 MPa, such as the Daofu–Kangding section fault, the northern part of the Kangding–Shimian section fault, and the Kangding–Mianning section fault.

Following the 2008 *Mw* 7.9 earthquake and 2013 *Mw* 6.6 Lushan earthquake, Coulomb stress increases with time were observed in the Daofu–Kangding segment of the Xianshuihe Fault (Shan et al., 2013; Shao et al., 2010), and the fault locking significantly increased with ISC from 0.5 to 0.9 (Li et al., 2022a). The high stress accumulation of >1 Mpa resulting from the long-term combination of historical earthquake and tectonic movements, coupled with the stress loading of the Luding earthquake (Fig. 6b) enhanced the seismic hazards of the segment fault. Although the Luding earthquake enhanced the Coulomb stress in the northern part of the Moxi Fault (Fig. 6b), the weakly locking zones with an ISC of <0.2 (Fig. 4g) possibly resulted from the continuous stress unloading of the 1955 M 7.5 earthquake (Fig. 7) makes it less prone to earthquakes. The 1480 M 7.5 event was the most recent earthquake (M > 7) in the Shimian–Mianning segment of the Anninghe Fault (Wen et al., 2008), and it has been >500 years since this event. The long-term tectonic movement loading causing the strong locking with an ISC of >0.8 (Fig. 4g) and the high stress accumulation of >1 MPa (Fig. 7) enhanced the future seismic hazards of the Anninghe Fault with the stress loading of the Luding event, which should be closely monitored.

5. Conclusions

Studying the coseismic displacement, deep-shallow slip distribution, and interseismic deformation mode is key to understanding the occurrence of strong earthquakes along large fault zones. In this study, the horizontal coseismic displacement for the 2022 Luding earthquake was estimated using GPS remeasurements. Coseismic slip distribution was determined under the constraint of GPS data. We analyzed the relationships between coseismic slip, historical seismicity, and interseismic deformation and concluded that tectonic movement played a dominant role in generating the Luding earthquake, and the main rupture area corresponded to the strong interseismic locking area. The stress accumulation in the northwest of the epicenter was low owing to the continuous unloading of the 1955 M 7.5 earthquake, which might have arrested the rupture propagation. The phenomenon of shallow slip deficit was identified in the Luding model. Field investigation determined the extensive surface rupture and landslide, indicating that the strong ground motion produced inelastic deformation responsible for a certain amount of shallow coseismic slip deficit. We calculated the coseismic Coulomb stress change of the Luding event. By combining historical seismicity and interseismic deformation, we determined that the seismic hazards of the Daofu–Kangding section of the Xianshuihe and the Shimian–Mianning section of the Anninghe faults were enhanced.

CRediT authorship contribution statement

Hongbao Liang: Writing – original draft, Project administration, Formal analysis, Data curation, Conceptualization. **Yanqiang Wu:** Writing – review & editing, Funding acquisition, Formal analysis. **Zhigang Shao:** Formal analysis, Data curation. **Jingwei Li:** Formal analysis, Data curation. **Yalun Li:** Data curation. **Songquan Yi:** Data curation. **Fan Yang:** Data curation. **Wenquan Zhuang:** Data curation. **Hua Wang:** Data curation. **Wei Zhan:** Writing – review & editing, Formal analysis, Data curation. **Changyun Chen:** Writing – review & editing, Formal analysis.

Declaration of Competing Interest

The authors declare that they have no known competing financial interests or personal relationships that could have appeared to influence the work reported in this paper.

Data availability

Data will be made available on request.

Acknowledgments

This study was supported by the National Key Research and Development Program of China (No. 2017YFC1500501) and the National Natural Science Foundation of China (No. 41974011). The authors are deeply grateful for the GPS data shared by the Crustal Movement Observation Network of China. Part of the GPS data analyzed in this study was provided by Prof. Xiong at the China University of Geosciences and supported by the National Science Foundation of China (No. 41731072). We are grateful to Qingyun Zhang, Yongkui Wan, Shuang Zhu, Yajin Pang, and Yongzhe Wang for their help in data processing and coseismic slip inversion. All figures presented in this manuscript were generated by the Generic Mapping Tools (Wessel et al., 2013).

References

Allen, C.R., Luo, Z., Qian, H., Wen, X., Zhou, H., Huang, W., 1991. Field study of a highly active fault zone: the Xianshuihe Fault of southwestern China. GSA Bull. 103 (9), 1178–1199. https://doi.org/10.1130/0016-7606(1991)103<1178:FSOAHA>2.3.CO;2.

Avouac, J.P., Meng, L.S., Wei, S.J., Wang, T., Ampuero, J.P., 2015. Lower edge of locked Main Himalayan Thrust unzipped by the 2015 Gorkha earthquake. Nat. Geosci. 8, 708–711. https://doi.org/10.1038/ngeo2518.

Bai, M., Chevalier, M.L., Leloup, P.H., Li, H., Pan, J., Replumaz, A., Wang, S., Li, K., Wu, Q., Liu, F., Zhang, J., 2021. Spatial slip rate distribution along the SE Xianshuihe fault, Eastern Tibet, and earthquake hazard assessment. Tectonics 40 (11). https://doi.org/10.1029/2021TC006985 e2021TC006985.

China Earthquake Networks Center CENC, 2022. Focal Mechanism. Retrieved from. https://www.cea.gov.cn/cea/dzpd/dzzt/5683568/5683579/5684087/index.html.

Deng, Q., Zhang, P., Ran, Y., Yang, X., Min, W., Chu, Q., 2003. Basic characteristics of active tectonics of China. Sci. China Ser. D Earth Sci. 46, 356–372. https://doi.org/10.1360/03ys9030.

Ding, K., He, P., Wen, Y., Chen, Y., Wang, D., Li, S., Wang, Q., 2018. The 2017 Mw 7.3 Ezgeleh, Iran earthquake determined from InSAR measurements and teleseismic waveforms. Geophys. J. Int. 215 (3), 1728–1738. https://doi.org/10.1093/gji/ggy371.

Fang, L., Wu, J., Liu, J., Cheng, J., 2015. Preliminary Report on the 22 November 2014 Mw6.1/Ms6.3 Kangding Earthquake, Western Sichuan, China. Seismol. Res. Lett. 86 (6) https://doi.org/10.1785/0220150006.

Feng, G., Sigurjón, S., 2012. Shortcomings of InSAR for studying megathrust earthquakes: The case of the Mw9.0 Tohoku-Oki earthquake. Geophys. Res. Lett. 39 https://doi.org/10.1029/2012GL051628. L10305.

Fialko, Y., Sandwell, D., Simons, M., Rosen, P., 2005. Three-dimensional deformation caused by the bam, Iran, earthquake and the origin of shallow slip deficit. Nature 435, 295–299. https://doi.org/10.1038/nature03425.

Freed, A.M., Lin, J., 2001. Delayed triggering of the 1999 Hector Mine earthquake by viscoelastic stress transfer. Nature 411, 180–183. https://doi.org/10.1038/35075548.

Global CMT Catalog Search GCMT, 2022. Earthquake catalog released by Global CMT Catalog Search. Retrieved from. https://www.globalcmt.org/CMTsearch.html.

Gomberg, J.S., Shedlock, K.M., Roecker, S.W., 1990. The effect of S-wave arrival times on the accuracy of hypocenter estimation. Bull. Seismol. Soc. Am. 80, 1605–1628.

Guo, R., Li, L., Zhang, W., Zhang, Y., Tang, X., Dai, K., Li, Y., Zhang, L., Wang, J., 2023. Kinematic slip evolution during the 2022 Ms 6.8 Luding, China, earthquake: Compatible with the preseismic locked patch. Geophys. Res. Lett. 50 https://doi.org/10.1029/2023GL103164 e2023GL103164.

He, P., Wang, Q., Ding, K., Wang, M., Qiao, X., Li, J., Wen, Y., Xu, C., Yang, S., Zou, R., 2016. Source model of the 2015 Mw 6.4 Pishan earthquake constrained by interferometric synthetic aperture radar and GPS: Insight into blind rupture in the western Kunlun Shan. Geophys. Res. Lett. 43, 1511–1519. https://doi.org/10.1002/2015GL067140.

Herring, T.A., King, R.W., Floyd, M.A., McClusky, S.C., 2018a. GAMIT Reference Manual. In: GPS Analysis at MIT (Release 10.7), Department of Earth, Atmosphere, and Planetary Sciences Massachusetts Institute Technology.

Herring, T.A., Floyd, M.A., King, R.W., McClusky, S.C., 2018b. GLOBK Reference Manual. In: Global Kalman filter VLBI and GPS analysis program (Release 10.7), Department of Earth, Atmosphere, and Planetary Sciences Massachusetts Institute Technology.

Huang, Y., Xie, C., Li, T., Xu, C., He, X., Shao, X., Xu, X., Zhan, T., Chen, Z., 2022. An open-accessed inventory of landslides triggered by the Ms 6.8 Luding earthquake, China on 5 September 2022. Earthq. Res. Advan. 3 (1), 100181. https://doi.org/10.1016/j.eqrea.2022.100181.

Jiang, Z., Wang, M., Wang, Y., Wu, Y., Che, S., Shen, Z.-K., et al., 2014. GPS constrained coseismic source and slip distribution of the 2013 Mw6.6 Lushan, China, earthquake and its tectonic implications. Geophys. Res. Lett. 41 https://doi.org/10.1002/2013GL058812.

Jiang, G., Xu, X., Chen, G., Liu, Y., Fukahata, Y., Wang, H., Yu, G., Tan, X., Xu, C., 2015. Geodetic imaging of potential seismogenicasperities on the Xianshuihe-Anninghe-Zemuhe fault system, southwest China,with a new 3-D viscoelastic interseismic ccoupling model. J. Geophys. Res. Solid Earth 120, 1855–1873. https://doi.org/10.1002/2014JB011492.

Jiang, P., Li, P., Li, T., Zeng, J., Wang, J., Su, J., Wen, R., 2023. The characteristics of strong motion records of the 2022 Luding, Sichuan Ms6.8 earthquake. J. Seismol. Res. (in Chin.) 46 (4), 593–602. https://doi.org/10.20015/j.cnki.ISSN1000-0666.2023.0057.

Jin, Z., Fialko, Y., 2021. Coseismic and early postseismic deformation due to the 2021 M7.4 Maduo (China) earthquake. Geophys. Res. Lett. 48 https://doi.org/10.1029/2021GL095213 e2021GL095213.

Kaneko, Y., Fialko, Y., 2011. Shallow slip deficit due to large strike-slip earthquakes in dynamic rupture simulations with elasto-plasticoff-fault response. Geophys. J. Int. 186, 1389–1403. https://doi.org/10.1111/j.1365-246x.2011.05117.x.

Kaneko, Y., Avouac, J.P., Lapusta, N., 2010. Towards inferring earthquake patterns from geodetic observations of interseismic coupling. Nat. Geosci. 3 (5), 363–369. https://doi.org/10.1038/ngeo843.

Kaneko, Y., Fialko, Y., Sandwell, D., Tong, X., Furuya, M., 2013. Interseismic deformation and creep along the central section of the North Anatolian Fault (Turkey): InSAR observations and implications for rate-and-state friction properties. J. Geophys. Res. 118, 316–331. https://doi.org/10.1029/2012jb009661.

Kato, N., Lei, X., Wen, X., 2007. A synthetic seismicity model for the 30ianshuihe fault, southwestern China: simulation using a rate- and state-dependent friction law. Geophys. J. Int. 169 (1), 286–300. https://doi.org/10.1111/j.1365-246X.2006.03313.x.

LaBonte, A., Brown, K., Fialko, Y., 2009. Hydrogeologic detection and finite-element modeling of a slow-slip event in the Costa Ricaprism toe. J. Geophys. Res. 114 https://doi.org/10.1029/2008JB005806. B00A02.

Li, Y., Nocquet, J.-M., Shan, X., Jian, H., 2021. Heterogeneous interseismic coupling along the XianshuiheXiaojiang fault system, eastern Tibet. J. Geophys. Res. Solid Earth 126. https://doi.org/10.1029/2020JB021187 e2020JB021187.

Li, L., Wu, Y., Li, Y., Zhan, W., Liu, X., 2022a. Dynamic deformation and fault locking of the Xianshuihe Fault Zone, Southeastern Tibetan Plateau: implications for seismic hazards. Earth Planets Space 74 (35). https://doi.org/10.1186/s40623-022-01591-9.

Li, C., Sun, K., Ma, J., Li, J., Liang, M., Fang, L., 2022b. The 2022 M6.8 Luding earthquake: a complicated event by faulting of the Moxi segment of the Xianshuihe fault zone. Seismol. Geol. (in Chinese) 44 (6), 1648–1666. https://doi.org/10.3969/j.issn.0253-4967.2022.06017.

Li, Y., Zhao, D., Shan, X., Gao, Z., Huang, X., Gong, W., 2022c. Coseismic slip model of the 2022 Mw 6.7 Luding (Tibet) earthquake: Preand post-earthquake interactions with surrounding major faults. Geophys. Res. Lett. 49 https://doi.org/10.1029/2022GL102043 e2022GL102043.

Liang, H., Zhan, W., Li, J., Zhu, S., 2022. Terrestrial reference frame SC20 for monitoring crustal deformation in the adjacent areas of the South China block. Geophys. J. Int. 229 (1), 426–438. https://doi.org/10.1093/gji/ggab483.

Liu, C., Lay, T., Xiong, X., 2022. The 29 July 2021 MW 8.2 Chignik, Alaska Peninsula Earthquake Rupture Inferred From Seismic and Geodetic Observations: Re-Rupture of the Western 2/3 of the 1938 Rupture Zone. Geophys. Res. Lett. 49 (4) https://doi.org/10.1029/2021GL096004 e2021GL096004.

Massonnet, D., Rossi, M., Carmona, C., Adragna, F., Peltzer, G., Feigl, K., Rabaute, T., 1993. The displacement field of the Landers earthquake mapped by radar interferometry. Nature 364 (6433), 138–142. https://doi.org/10.1038/364138a0.

Qiao, X., Zhou, Y., 2021. Geodetic imaging of shallow creep along the Xianshuihe fault and its frictional properties. Earth Planet. Sci. Lett. 567, 117001. https://doi.org/10.1016/j.epsl.2021.117001.

Robinson, R., Zhou, S.Y., 2005. Stress interaction within the Tangshan, China, earthquake sequence of 1976. Bull. Seismol. Soc. Am. 95 (6), 2501–2505. https://doi.org/10.1785/0120050091.

Savage, J.C., Burford, R., 1973. Geodetic determination of relative plate motion in Central California. J. Geophys. Res. 95, 4873–4879. https://doi.org/10.1029/JB078i005p00832.

Schwartz, D.P., Coppersmith, K.J., 1984. Fault behavior and characteristic earthquakes examples from the Wasatch and San Andreas Fault zones. J. Geophys. Res. 90, 5681–5698. https://doi.org/10.1029/JB089iB07p05681.

Shan, B., Xiong, X., Zheng, Y., Jin, B., Liu, C., Xie, Z., Xu, H., 2013. Stress changes on major faults caused by 2013 Lushan earthquake, and its relationshipin with 2008 Wenchuan earthquake. Sci. China:Earth Science 43, 1002–1009. https://doi.org/10.1007/s11430-013-4642-1.

Shao, Z., Zhou, L., Jiang, C., Ma, H., Zhang, L., 2010. The impact of Wenchuan MS8.0 earthquake on the seismic activity of surrounding faults. Chin. J. Geophys. (in Chinese) 53 (8), 1784–1795. https://doi.org/10.3969/j.issn.0001-5733.2010.08.004.

She, Y., Fu, G., Xu, C., 2022. Seasonal terrestrial water load modulation of seismicity at the southeastern margin of the Tibetan Plateau constrained by GNSS and GRACE data. Geophys. J. Int. 230 (3), 1966–1979. https://doi.org/10.1093/gji/ggac168.

Shen, Z.K., Lü, J., Wang, M., Bürgmann, R., 2005. Contemporary Crustal deformation around the Southeast borderland of the Tibetan Plateau. J. Geophys. Res. Solid Earth 110 (B11), B114409. https://doi.org/10.1029/2004JB003421.

Shimazaki, K., Nakata, T., 1980. Time-predictable recurrence model for large earthquakes. Geophys. Res. Lett. 7 (4), 279–282. https://doi.org/10.1029/GL007i004p00279.

Song, X., Zhang, Y., Shan, X., Liu, Y., Gong, W., Qu, C., 2019. Geodetic observations of the 2018 Mw 7.5 Sulawesi earthquake and its implications for the kinematics of the Palu fault. Geophys. Res. Lett. 46, 4212–4220. https://doi.org/10.1029/2019gl082045.

Tapponnier, P., Xu, Z., Roger, F., Meyer, B., Arnaud, N., Wittlinger, G., Yang, J., 2001. Oblique stepwise rise and growth of the Tibet Plateau. Science 294 (5547), 1671–1677. https://doi.org/10.1126/science.105978.

Toda, S., Stein, R.S., 2020. Long-and short-term stress interaction of the 2019 Ridgecrest sequence and Coulomb-based earthquake forecasts. Bull. Seismol. Soc. Am. 110 (4), 1765–1780. https://doi.org/10.1785/0120200169.

U. S. Geological Survey USGS, 2022. Earthquake Catalog Released by U. S. Geological Survey. Retrieved from. https://earthquake.usgs.gov/earthquakes/eventpage/us7000i59t/moment-tensor.

Vaca, S., Vallée, M., Nocquet, J.M., Battaglia, J., Régnier, M., 2018. Recurrent slow slip events as a barrier to the northward rupture propagation of the 2016 Pedernales earthquake (Central Ecuador). Tectonophysics 724, 80–92. https://doi.org/10.1016/j.tecto.2017.12.012.

Wan, Y., Liu, Xia, Liu, R., Zhang, Y., Shen, X., Zheng, Z., 2022. Numerical simulation of the present deformation pattern in the crust and top of the upper Mantle in the Songpan-Garze block. Chin. J. Geophys. 65 (7), 2484–2502. https://doi.org/10.6038/cjg2022P0235.

Wang, M., Shen, Z., 2020. Present-day crustal deformation of continental China derived from GPS and its tectonic implications. J. Geophys. Res. Solid Earth 125. https://doi.org/10.1029/2019JB018774 e2019JB018774.

Wang, R., Lorenzo-Martin, F., Roth, F., 2006. PSGRN/PSCMP – a new code for calculating co- and post-seismic deformation, geoid and gravity changes based on the viscoelastic-gravitational dislocation theory. Comput. Geosci. 32 (4), 527–541.

Wang, S., Fan, C., Wang, G., Wang, E., 2008. Late Cenozoic deformation along the northwestern continuation of the Xianshuihe fault system. Eastern Tibetan Plateau. *GSA*. Bulletin 120 (3–4), 312–327. https://doi.org/10.1130/B25833.1.

Wang, R., Diao, F., Hoechner, A., 2013. SDM-A Geodetic Inversion Code Incorporating with Layered Crust Structure and Curved Fault Geometry. //EGU General Assembly 2013. Vienna. EGU, Austria.

Wei, S., Barbot, S., Graves, R., Lienkaemper, J.J., Wang, T., Hudnut, K., et al., 2015. The 2014 Mw 6.1 South Napa earthquake: a unilateral rupture with shallow asperity and rapid afterslip. Seismol. Res. Lett. 86, 344–354. https://doi.org/10.1785/0220140249.

Wen, X., Ma, S., Xu, X., He, Y., 2008. Historical pattern and behavior of earthquake ruptures along the eastern boundary of the Sichuan-Yunnan faulted-block, southwestern China. Phys. Earth Planet. Inter. 168 (1–2), 16–36. https://doi.org/10.1016/j.pepi.2008.04.013.

Wessel, P., Smith, W.H., Scharroo, R., Luis, J., Wobbe, F., 2013. Generic mapping tools: improved version released. EOS Trans. Am. Geophys. Union 94 (45), 409–410. https://doi.org/10.1002/2013eo450001.

Wu, Y., Jiang, Z., Yang, G., Wei, W., Liu, X., 2011. Comparison of GPS strain rate computing methods and their reliability. Geophys. J. Int. 185, 703–717. https://doi.org/10.1111/j.1365-246X.2011.04976.x.

Wu, Y., Jiang, Z., Pang, Y., Chen, C., 2021. Statistical correlation of seismicity and geodetic strain rate in the Chinese mainland. Seismol. Res. Lett. 93 (1), 268–276. https://doi.org/10.1785/0220200048.

Wu, Y., Zheng, Z., Nie, J., Chang, L., Su, G., Yin, H., et al., 2022. Highprecision vertical movement and three-dimensional deformation pattern of the Tibetan Plateau. J. Geophys. Res. Solid Earth 127. https://doi.org/10.1029/2021JB023202 e2021JB023202.

Xu, X., Tong, X., Sandwell, D.T., Milliner, C.W.D., Dolan, J.F., Hollingsworth, J., Leprince, S., Ayoub, F., 2016. Refining the shallow slip deficit. Geophys. J. Int. 204 (3), 1867–1886. https://doi.org/10.1093/gji/ggv563.

Xu, W., Feng, G., Meng, L., Zhang, A., Ampuero, J.P., Bürgmann, R., Fang, L., 2018. Transpressional rupture cascade of the 2016 Mw 7.8 Kaikoura earthquake, New Zealand. J. Geophys. Res. Solid Earth 123, 2396–2409. https://doi.org/10.1002/2017JB015168.

Xu, J., Shao, Z., Li, J., Ji, L., 2019. Coulomb stress evolution and future earthquake probability along the eastern boundary of the Sichuan-Yunnan block. Chin. J. Geophys. (in Chinese) 62 (11), 4189–4213. https://doi.org/10.6038/cjg2019M0593.

Zhang, Q., Li, Y., Zhang, J., Tian, Y., Tian, T., Li, B., 2023a. Slip deformation along the Gyaring Co fault from InSAR and GPS. Acta Geophys. 71, 53–63. https://doi.org/10.1007/s11600-022-00920-6.

Zhang, L., Zhou, Y., Zhang, X., Zhu, A., Li, B., Wang, S., Liang, S., Jiang, C., Wu, J., Li, Y., Su, J., Yan, L., Fang, L., 2023b. 2022 Mw 6.6 Luding, China, earthquake: a strong Continental Event Illuminating the Moxi Seismic Gap. Seismol. Res. Lett. https://doi.org/10.1785/0220220383.

Zhao, B., Qi, Y., Wang, D., Yu, J., Li, Q., Zhang, C., 2018. Coseismic Slip Model of the 2018 Mw 7.9 Gulf of Alaska Earthquake and its Seismic Hazard Implications. Seismol. Res. Lett. 90 (2A), 632–648. https://doi.org/10.1785/0220180141.

Zhao, J., Ren, J., Liu, J., Jiang, Z., Liu, X., Liang, H., Niu, A., Yue, C., Yuan, Z., 2020. Coupling fraction and relocking process of the Longmenshan fault zone following the 2008 Mw 7.9 Wenchuan earthquake. J. Geodyn. 137, 101730. https://doi.org/10.1016/j.jog.2020.101730.